

Faithful Tight-binding Models and Fragile Topology of Magic-angle Bilayer Graphene

Hoi Chun Po,¹ Liujun Zou,^{1,2} T. Senthil,² and Ashvin Vishwanath¹

¹*Department of Physics, Harvard University, Cambridge, MA 02138, USA*

²*Department of Physics, Massachusetts Institute of Technology, Cambridge, MA 02139, USA*

Correlated insulators and superconductivity have been observed in “magic-angle” twisted bilayer graphene, when the nearly flat bands close to neutrality are partially filled. While a momentum-space continuum model accurately describes these flat bands, interaction effects are more conveniently incorporated in tight-binding models. We have previously shown that no fully symmetric tight-binding model can be minimal, in the sense of capturing just the flat bands, so extended models are unavoidable. Here, we introduce both a six- and a ten-band tight-binding model that capture the flat bands while simultaneously retaining all symmetries. These models are also faithful, in that the additional degrees of freedom represent energy bands further away from neutrality, and they serve as optimal starting points for a controlled study of interaction effects. Furthermore, our construction demonstrates the “fragile topology” of the nearly flat bands, i.e. they can be reduced to exponentially localized Wannier functions if and only if a particular set of trivial bands are added to the model.

I. INTRODUCTION

In strongly correlated materials such as transition metal oxides, which include the high- T_c cuprate materials [1], the competition between kinetic energy and electron-electron interactions stabilizes remarkable phases such as Mott insulators and high-temperature superconductors. Their theoretical description traditionally begins with a tight-binding model which provides a real-space representation of the relevant electronic bands. Interactions are then incorporated by means of a local U term, leading to the Hubbard model.

Recently, another example of a correlated insulator in proximity to a superconductor has appeared—two adjacent graphene sheets that are twisted by a specific small angle relative to each other [2, 3]. Here, we will address the question of constructing a minimal model for twisted bilayer graphene, analogous to the square-lattice tight-binding model for cuprates. We will see that traditional approaches to this problem fail due to a form of band topology inherited from the underlying Dirac nature of the problem. Instead, a new approach is called for, which is developed in this paper.

Twisted bilayer graphene (TBG) structures have been studied intensely in the last decade [4–27]. To begin with, the two valleys of graphene are decoupled from one another, particularly in the limit of small twist angles, yielding a valley quantum number in addition to spin. The electronic states near each valley of each graphene monolayer hybridize with the corresponding states from the other monolayer. When the twist angle is close to certain discrete values known as the magic angles, e.g., at $\sim 1.05^\circ$, theoretical calculations show that there are two nearly flat bands (per valley and per spin) that form in the middle of the spectrum [12] and are separated from other bands [24]. The band gaps are also observed in experiments [2, 3]. These nearly flat bands contain Dirac nodes that intersect the chemical potential at neutrality.

Counting electron filling from neutrality, at fillings $\nu_T = \pm 4$ a band insulator is obtained. However, in experiments, correlated insulators are observed at partial band fillings of $\nu_T = \pm 2$ on cooling below a few Kelvin. Further doping this insulator at $\nu_T = -2$ with either electrons or holes reveals superconductivity at a $T_c \sim 1$ K [3]. A natural question that arises is:

how similar is this phenomenon to that in the cuprates, and, relatedly, what is the minimal model that we should consider here, analogous to the square-lattice Hubbard model for the cuprates?

Ideally, a minimal tight-binding model for TBG would describe *only* the two nearly flat bands (per valley and per spin) and respect all symmetries. However, there is an interesting topological aspect to the nearly flat bands that obstructs finding such a model [28, 29]. This is intuitively seen by recognizing that the two Dirac points in the nearly flat bands originate from the unperturbed Dirac cones which, while living in different layers, belong to the same valley. This suggests that they carry the same chirality [2, 13, 15, 30], i.e. the same Berry phase of $\pm\pi$ of the two Dirac cones, whose relative sign is well-defined. In contrast, any two-band tight-binding model would give Dirac cones with vanishing net chirality. This obstruction is also reflected in the symmetry eigenvalues of the bands, which cannot be captured in a minimal two-band tight-binding model [28, 29]. Given that a minimal tight binding model is forbidden, one must then proceed with one of the following two options (i) extend the model to include additional bands, *or* (ii) give up on some symmetries.

In this paper we will pursue the first option, namely, forgoing the minimality requirement and constructing models with more than two bands. Specifically, we will introduce a ten-band model in which the connected bands follow a 4-2-4 sequence, with the middle two bands representing the nearly flat bands of a single valley of TBG. Our model has the following advantages. First, all symmetries are respected and represented appropriately, and the two isolated bands incorporate the previously mentioned band topology of TBG. Second, the additional, complementary bands have a natural correspondence with the higher-energy bands in TBG. Finally, we can incorporate an approximate particle-hole symmetry in this description, which is known to be a good symmetry for the higher-energy states (although generally broken for the nearly flat bands). We also discuss the construction of a more minimal six-band model which retains a set of four excited bands only on one side of the nearly flat bands. Our models therefore pave the way to the derivation of a symmetric, interacting real-space description of TBG. Our solutions are reminiscent of ‘p-d’ models of the copper oxides, where corre-

lated ‘d’ copper orbitals are augmented by oxygen ‘p’ orbitals [31]. An important difference here is that the topological obstruction prevents further downfolding that would eliminate the additional bands.

Furthermore, the complementary bands in our model are manifestly *trivial*, in that they can be smoothly deformed into an explicit atomic insulator. This is conceptually interesting, as it is in stark contrast with the familiar forms of band topology, say those exemplified by the Haldane [32] or Kane-Mele [33, 34] models, which are described by stable (K-theoretic) topological invariants [35–37]. There, the nontrivial topological indices must cancel when all sets of bands are accounted for, so a band with stable topology cannot be neutralized by additional trivial bands. Rather, our model proves that the identified band topology in TBG falls into the class of “fragile topology” recently introduced in Ref. 38.

Let us also mention that, in Ref. 29, we provided a different recipe to extend the model. There, we constructed a four-band model where all the symmetries are implemented naturally, and the four bands split into 2-2 sets of isolated bands, each of which individually showcases the identified band topology of TBG. While the smaller number of bands is an advantage, the additional bands are disconnected from the physical degrees of freedom in TBG, and interactions can be reliably treated only when they are weak enough that interband mixing can be safely neglected. In contrast, we believe our present solution is superior in that the additional degrees of freedom correspond to physical excited states, and that it clarifies the fragile nature of the band topology.

The second option for constructing effective tight-binding models, which we recall by way of review, is to circumvent the Wannier obstructions by implementing some of the symmetries in a nontrivial manner [28]. This was done for valley symmetry in Ref. [28], which, however, entails a non-standard procedure to eventually recover the symmetry, unlike the option discussed here. Alternately, one can simply ignore some symmetries in the problem [39–41], or to adopt some different implementations of the symmetries [42–46]. An unintended consequence is a need for fine tuning. Hence, the theoretical predictions of these models are not automatically justified. For instance, in the symmetry setting of Refs. 39–41 a vertical electric field would lead to a band gap at charge neutrality, which is inconsistent with that dictated by the actual symmetries of the system [4].

We begin by briefly reviewing the symmetries and band topology relevant for small-angle TBG, before defining our ten- and six-band models, and providing a physical picture for their construction. Finally we discuss the fragile topology of the TBG flat bands and close with a discussion. Henceforth, we will focus on the single-valley problem with spin ignored.

II. SYMMETRY AND TOPOLOGY OF TBG

In the following, we focus on the symmetries of the continuum description [4, 12], which are also exact for the highest-symmetry commensurate lattice realizations [7, 8, 14, 29]. A more thorough review of these topics can be found in Ref. 29.

TABLE I. Symmetry representations furnished by the nearly flat bands of twisted bilayer graphene [28, 29], indicated by the eigenvalues of the generating symmetries of the point group. Eigenvalues from degenerate bands are grouped by parenthesis.

| Eig. | Γ | K |
|-------|----------|----------------------|
| C_3 | 1, 1 | (ω, ω^*) |
| M_y | 1, -1 | not a symmetry |

The spatial symmetry group of TBG is generated by lattice translations, C_6 rotation, and a 2D mirror M_y which flips the y coordinate (more accurately, a layer-exchanging two-fold rotation in 3D)¹. It is also symmetric under time-reversal \mathcal{T} . In addition, at small twist angle the two valleys are effectively decoupled, leading to an additional $U_v(1)$ valley charge conservation. This allows one to consider the electronic degrees of freedom residing in a single valley. Among the listed symmetries, only C_6 and \mathcal{T} exchange the two valleys; all the others, as well as the combinations like $C_6\mathcal{T}$, leave the valley charge invariant. Consequentially, the (magnetic) point group of the single-valley problem is generated by $C_6\mathcal{T}$ and M_y , and the problem is described by the magnetic space group 183.188 (in the BNS notation) [28].

One can readily compute the symmetry representations furnished by the two nearly flat bands at different high-symmetry momenta, which we list in Table I. Importantly, one can check that *no* atomic insulator with the same symmetries will have the same set of symmetry representations (Appendix A), and therefore there is an obstruction for constructing symmetric Wannier functions for the two nearly flat bands. This alone implies the two relevant bands are topologically obstructed from any tight-binding description that respects all symmetries [28]. In addition, unlike the familiar case of monolayer graphene [30], the two Dirac points in the TBG band structures have the *same* chirality [2, 13, 15, 30]. This is impossible in any two-band tight-binding model and constitutes another Wannier obstruction [28]. Curiously, the two mentioned obstructions, derived respectively from the representations of M_y and the net chirality of the Dirac points, are intertwined: it was shown in Ref. 29 that when the only Dirac points are pinned to the two (moiré) K points, the mirror and chirality obstructions are equivalent.

III. TIGHT-BINDING MODELS

A. A ten-band model

Let us now describe the mentioned ten-band model. In our present symmetry setting, one can label the orbitals as being

¹ Note that M_y may not be present in the actual experiment, due to, for instance, different processing of the top and bottom layers. Nonetheless, as long as its (explicit) breaking is perturbative, it will be helpful to retain it as a theoretical crutch.

TABLE II. Orbital content of the ten-band model. τ , κ , and η respectively denote the triangular, kagome, and honeycomb sites. s_{\pm} and p_{\pm} denote different orbital characters. One can also construct a more minimal six-band model using only the orbitals listed to the left of the double vertical line.

| Orbitals | (τ, p_z) | (τ, p_{\pm}) | (κ, s) | (η, p_{\pm}) |
|--------------|---------------|-------------------|---------------|-------------------|
| No. of bands | 1 | 2 | 3 | 4 |

either s , p_z , or p_{\pm} . Both s and p_z orbitals transform trivially under a C_3 rotation, but p_z flips sign under M_y while s does not². In contrast, the orbitals $p_{\pm} = p_x \pm ip_y$ are exchanged under M_y and form a doublet. A more systematic tabulation of the symmetry properties of the orbitals can be found in Appendix A. Our ten-band model comprises a p_z orbital and a pair of p_{\pm} orbitals localized to sites forming a triangular lattice (τ), a s orbital on the kagome lattice (κ), and a pair of p_{\pm} orbitals forming a honeycomb lattice (η). For brevity, we will describe the orbital content using the notation (lattice, orbital), e.g., (τ, p_z) denotes the p_z orbitals localized to the triangular site. Similarly, we denote the associated fermion operator by $\hat{c}_{p_{\pm}}$. The described degrees of freedom are tersely summarized in Table II in this notation.

A prerequisite for any tight-binding modeling of TBG is the capability of producing two isolated bands with the targeted momentum-space symmetry representations (Table I). This is guaranteed in our model by the following representation-matching equation:

$$(\tau, p_z) \oplus (\tau, p_{\pm}) \oplus (\kappa, s) \stackrel{\text{rep.}}{=} (\eta, p_{\pm}) \oplus (\text{target}), \quad (1)$$

which one can verify using the comprehensive tabulation of the symmetry data in Appendix A. The physical meaning of Eq. (1) is that, representation-wise, it is possible to construct an atomic insulator, with the same symmetry properties as (η, p_{\pm}) , within the six-band sub-Hilbert space defined by the content on the left-hand side. In our ten-band model, we add another, explicit set of (η, p_{\pm}) orbitals to both sides of the above equation, so that the full representation-matching equation reads

$$(\tau, p_z) \oplus (\tau, p_{\pm}) \oplus (\kappa, s) \oplus (\eta, p_{\pm})_0 \stackrel{\text{rep.}}{=} (\eta, p_{\pm})_1 \oplus (\text{target}) \oplus (\eta, p_{\pm})_2. \quad (2)$$

Note that we have added subscripts 0-2 to clarify that they represent different sets of physical degrees of freedom despite sharing identical symmetry properties.

Guided by this observation, one can construct a model with the targeted representations simply through the construction of the mentioned atomic insulator. Let \hat{c}_r^{\dagger} be the six-component fermion creation operators for the orbitals assigned to the unit cell at \mathbf{r} (Fig. 1a). We want to construct

a localized ‘‘quasi-orbital’’ wave function $h_{p_{\pm};\mathbf{r}}^{(l)}(\mathbf{x})$ such that $\hat{h}_{p_{\pm};\mathbf{r}}^{(l)\dagger} \equiv \sum_{\mathbf{x}} \hat{c}_{\mathbf{x}}^{\dagger} h_{p_{\pm};\mathbf{r}}^{(l)}(\mathbf{x})$ has the same symmetry properties as a p_{\pm} orbital centered at a *honeycomb site*, labeled by $l = A, B$ in the unit cell \mathbf{r} . This can be achieved by using a trial wave function which vanishes everywhere except on the three nearest kagome and triangular sites surrounding the honeycomb site. Site symmetries reduce the freedom in the wave function to four real parameters³, which we denote by a through d (Fig. 1b). Once $\hat{h}_{p_{+};\mathbf{r}}^{(l)\dagger}$ is specified, we can generate $\hat{h}_{p_{-};\mathbf{r}}^{(l)\dagger}$ centered at the same site, as well as those centered on the other sites, by symmetries. Note that we have *not* imposed orthogonality between the $h_{p_{\pm};\mathbf{r}}^{(l)}(\mathbf{x})$ wave functions, and so their associated fermion operators do not obey the canonical anti-commutation relations.

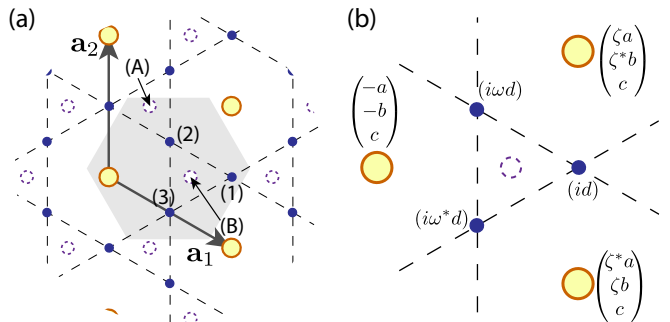


FIG. 1. Real-space orbitals. (a) Lattices and conventions. The shaded region indicates the relative positions of the sites assigned to the same unit cell. (b) The constructed quasi-orbital $h_{p_{+}}^{(B)}$ in the real space. $\zeta = e^{i2\pi/6}$ and $\omega = \zeta^2$. Going from top to bottom, the entries in the three-component vectors attached to the triangular sites denote the amplitude for the p_z , p_{+} and p_{-} orbitals; that attached to the kagome sites denote the amplitude of their associated s orbital.

We are now ready to define the ten-band model. Recall, in the above, we have not utilized the $(\eta, p_{\pm})_0$ orbitals in the system. Since they have identical symmetry properties as the $\hat{h}_{p_{\pm};\mathbf{r}}^{(l)\dagger}$ quasi-orbitals we constructed, we can couple the two sets in a minimal manner:

$$\hat{H}(t, \delta) = t \sum_{\mathbf{r}, l=A, B, \rho=p_{\pm}} (\hat{\eta}_{\rho;\mathbf{r}}^{(l)\dagger} \hat{h}_{\rho;\mathbf{r}}^{(l)} + \text{h.c.}) + \delta \hat{V}, \quad (3)$$

where t is a real parameter, \hat{V} is a symmetry-allowed, local perturbation which we detail in Appendix B, and the dimensionless parameter $\delta \in [0, 1]$ controls the overall strength of the perturbation. Note that the finite range of the wave functions $h_{p_{\pm};\mathbf{r}}^{(l)\dagger}$ imply \hat{H} is local. If the $h_{p_{\pm};\mathbf{r}}^{(l)\dagger}$ wave functions were orthonormal, $\hat{H}(t, 0)$ would be on-site and could be readily diagonalized through the bonding and anti-bonding of the $\eta_{p_{\pm}}$ and $h_{p_{\pm}}$ (quasi-)orbitals. The actual band structure of $\hat{H}(t, 0)$

² Recall, our ‘‘mirror’’ M_y is really a two-fold rotation in 3D.

³ Or four complex parameters if we lift some fictitious symmetry constraints (Appendix B); one less if we also impose normalization.

is shown in Fig. 2a, and it can be readily interpreted as a slight dressing of the bonding/ anti-bonding picture.

Importantly, by construction the band structure of $\hat{H}(t, 0)$ includes two exactly flat bands pinned at zero energy (Fig. 2d; see also Appendix B), whose symmetry representations must match those of the nearly flat bands in TBG. Very briefly, these flat bands exist here for the same geometric reason as that of the Lieb lattice [47]. In addition, we have chosen the wave function parameters a - d , listed in the caption of Fig. 2, to reproduce the broad energetic features of the higher-energy bands of TBG. Note that our model reproduces the approximate $E_{\mathbf{k}} = -E_{-\mathbf{k}}$ particle-hole symmetry of the higher energy states in TBG, although this is not a good symmetry of the nearly flat bands. With all the key properties built-in, we simply choose \hat{V} such that $\hat{H}(t, \delta)$ faithfully captures the energetics of the ten bands near charge neutrality in TBG. This leads to the band structure shown in Fig. 2b, which closely resembles that computed using the continuum theory of TBG (Fig. 2c). In particular, the two bands near charge neutrality in Fig. 2e touches only at the Dirac points pinned at K and K', just like that from the continuum theory (Fig. 2f). As they furnish the targeted symmetry representations in Table I, from the results in Ref. 29 they must display both the mirror and chirality Wannier obstructions, i.e., this ten-band model serves as an explicit resolution of all the known Wannier obstructions of the nearly flat bands of TBG.

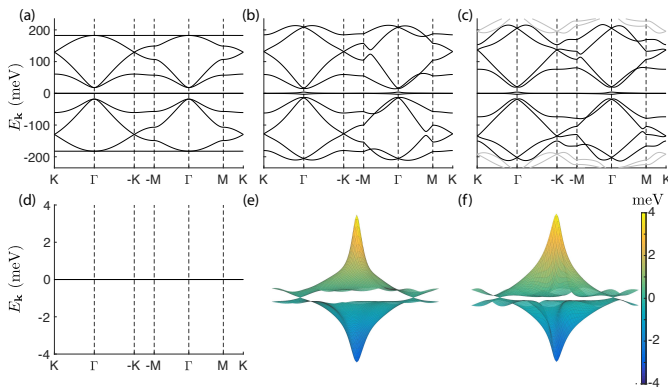


FIG. 2. Band structures. (a,b) Bands from the ten-band Hamiltonian $\hat{H}(t_0, \delta)$. For both panels, we choose $t_0 \equiv 130$ meV, and the wave-function parameters $(a, b, c, d) = (0.110, 0.033, 0.033, 0.573)$. We set $\delta = 0$ in (a) and 1 in (b). (c) Bands obtained from the continuum theory [4, 12] for twisted bilayer graphene with a twist angle of $\theta = 1.05^\circ$, using the parameters described in Ref. 41. The ten bands around charge neutrality are highlighted. (d-f) A zoom-in of the two bands at charge neutrality for the corresponding panels in (a-c). The three-dimensional plots in (e,f) are plotted over the first Brillouin zone centered at Γ , showing the presence of exactly two Dirac points pinned to K and K' = -K. Note that (e) is generated from our tight-binding model, whereas (f) is generated from the continuum model.

B. A six-band model

As the dominant term in the ten-band model in Eq. (3) can be viewed as a minimal coupling between the η and h degrees of freedom, one could imagine the consequences of “integrating out” the η fermions, which results in a low-energy theory described in terms of the h degrees of freedom. In our band-theory context, such a procedure can be done simply by adding an arbitrarily large chemical potential to η , which amounts to removing the four η bands from the Hilbert space. This leads to a six-band low-energy Hilbert space with the orbital content on the left-hand side of Eq. (1), but with the dominant kinetic term involving only the four bands arising from the h quasi-orbitals, i.e., there will again be two nearly flat bands near zero-energy.

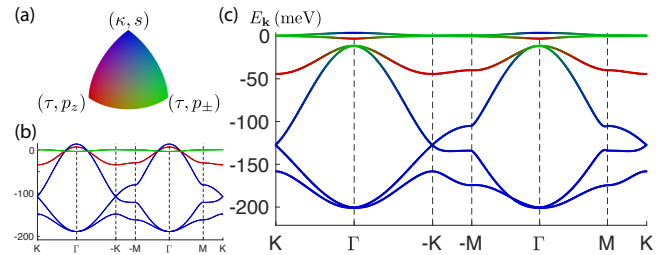


FIG. 3. Band structures from a six-band model. (a) Color code for the orbital characters. (b) The broad energetic features can be set up using only the intra-orbital dispersion. (c) Band structure from the full model, with parameters detailed in Appendix B 1.

While the preceding picture explains the existence of a six-band model, it is also desirable to construct such a model in a more conventional manner in terms of mostly nearest neighbor bonds. We will undertake this task below. Recall that the electron density of the nearly flat bands in TBG is localized to the “AA” regions, which form a triangular lattice at the moiré scale [5, 6, 11, 16, 20–22]. This suggests a tight-binding model with two orbitals placed on the triangular site. To capture the existence of Dirac points at K and K', these orbitals should be p_{\pm} , and naturally we anticipate the nearly flat bands to overlap strongly with the (τ, p_{\pm}) orbitals in most of the Brillouin zone. However, the (τ, p_{\pm}) bands feature an additional quadratic touching⁴ at the Gamma point, which cancels the Dirac-point chirality. In contrast, in TBG the two nearly flat bands are non-degenerate at Γ , and so the (τ, p_{\pm}) bands alone are incapable of capturing the Γ -point behavior [28, 39]. Therefore, we expect strong hybridization between the other orbitals in the vicinity of Γ , such that the wave function of the two nearly flat bands correspond to the singlet representations in (τ, p_z) and (κ, s) .

Based on the above picture, we construct a six-band model which captures all the salient feature of TBG, as we show in Fig. 3 and elaborate on in Appendix B 1.

⁴ which could split into multiple Dirac cones when trigonal warping is incorporated

IV. FRAGILE TOPOLOGY

We have presented two tight-binding models, with ten or six bands, each containing two isolated bands with all the known band topology in TBG. At a glimpse, this might appear to follow the general phenomenology of topological bands, which can only arise in a tight-binding model when the topological invariants are neutralized by complementary bands possessing the “opposite topology.” Paradoxically, the complementary bands in our model are constructed using quasi-orbitals h which correspond to an atomic insulator. This indicates that the complementary bands in the ten-band model $\hat{H}(t, \delta)$ are all trivial, in that they can be smoothly deformed into explicit atomic insulators. More precisely, we will demonstrate this following a trick described in Ref. 38, which relies on a deformation Hamiltonian

$$\hat{H}'_{\mu} = \hat{H}(f_{\mu} t_0, f_{\mu}^2) + \mu \sum_{r,l=A,B,\rho=p_{\pm}} \left(\frac{1}{10} \hat{\eta}_{\rho;r}^{(l)\dagger} \hat{\eta}_{\rho;r}^{(l)} - \hat{h}_{\rho;r}^{(l)\dagger} \hat{h}_{\rho;r}^{(l)} \right), \quad (4)$$

where we choose the dimensionless function $f_{\mu} = \cos(\pi\mu/2\mu_0)$ such that $f_0 = 1$ and $f_{-\mu_0} = f_{\mu_0} = 0$, implying $\hat{H}'_{\mu=0} = \hat{H}(t_0, 1)$. Note that the numerical factor of $1/10$ is *ad hoc* and is included simply to match the energy scales of the band gaps. Similarly, the precise form of f_{μ} , as well as the appearance of f_{μ}^2 , have little physical meaning; these are just convenient choices that suffice for our purpose. For $\mu = \mu_0 > 0$, the four highest bands coincide exactly with the atomic insulator arising from the full-filling of the $\eta_{p_{\pm}}$ orbitals, and the same is true for the four lowest bands when $\mu = -\mu_0$. As shown in Fig. 4a, the two band gaps in the spectrum never collapse for all $\mu \in [-\mu_0, \mu_0]$. This provides the needed adiabatic deformation to the explicit atomic limits (Fig. 4b).

Curiously, as both the full tight-binding model as well as the complementary bands correspond to atomic insulators, the band topology of the two nearly flat bands conform to the following equation:

$$(\text{trivial}) = (\text{trivial}') \oplus (\text{nontrivial}), \quad (5)$$

where we say a set of bands is trivial if and only if they admit a full set of symmetric, localized Wannier functions, i.e., the full-filling of which leads to an insulator which can be smoothly deformed into a strict atomic limit [48–51]. Eq. (5) is the defining property of “fragile topology” [38, 52, 53]. More concretely, we say the band topology of a set of gapped nontrivial bands is fragile if and only if one can append to the set another trivial set of bands such that, altogether, the augmented set is trivial; otherwise, we say the band topology is stable. As defined, stable and fragile topology are mutually exclusive concepts [38].

Since the band topology of our ten-band model conforms to Eq. (5), our model also serves to prove that the identified form of band topology is fragile in nature. For completeness, in Appendix C we establish the band topology in our six-band model is also fragile. This suggests that the interesting correlated behavior observed in TBG [2, 3] could be related to

interacting electrons occupying bands with an unconventional form of band topology.

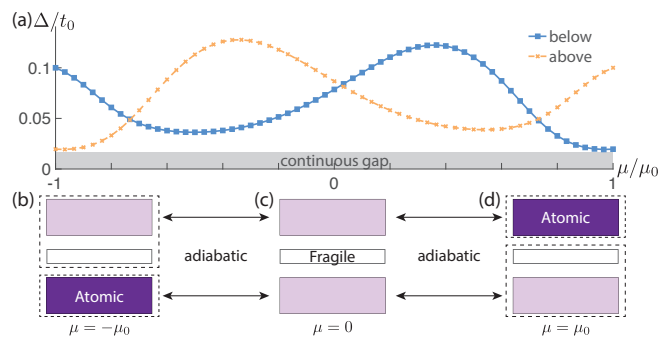


FIG. 4. Deformation to atomic limits. (a) The band gaps Δ below and above the two nearly flat bands stay open for all values of $\mu \in [-\mu_0, \mu_0]$ in Eq. (4). More than 3.6×10^4 momenta are sampled in the Brillouin zone in determining Δ . We choose $\mu_0 = t_0 = 130$ meV. (b–d) Schematic band diagrams at various limits of the deformation. (b) When $\mu = -\mu_0$, the lowest four bands arise solely from the (η, p_{\pm}) orbitals and are therefore strictly atomic. Correspondingly, the upper six bands, altogether, are also in a strict atomic limit. (Dashed boxes indicate strictly atomic bands.) The same is true for the case of $\mu = \mu_0$ in (d), but with the role of the lowest and highest bands exchanged. Since the band gaps are maintained throughout the entire deformation, we can infer that all the (light and dark) purple blocks correspond to trivial, atomic bands. The nearly flat bands at charge neutrality, therefore, must feature fragile topology.

As a conceptual remark, we note that the fragile phenomenology of our models will persist as long as we retain $C_2\mathcal{T}$ and lattice translations—the symmetries protecting the Dirac points. Therefore, upon the breaking of M_y and C_3 , our models provide an example of fragile topology not diagnosable using methods reliant on symmetry representations [50, 51].

V. DISCUSSION

In this work, we prove that the identified form of band topology in TBG is “fragile” in nature [38], and could be resolved simply by the addition of trivial degrees of freedom. This is accomplished by the construction of explicit tight-binding models that faithfully capture all the key energetic, symmetry and topology features of the bands near charge neutrality. Our results are based on the observation encapsulated in Eq. (1) and its similarity with Eq. (5), where the latter is the defining phenomenology of fragile topology. However, we caution that such representation-matching equations are not unique (see Appendix A for more details). For instance, one can interchange $s \leftrightarrow p_z$ in Eq. (1) and it still holds. Alternatively, one might also swap some of the orbitals used through the equality $(\tau, p_z) \oplus (\tau, p_{\pm}) \stackrel{\text{rep.}}{=} (\kappa, s)$ (and similarly with $s \leftrightarrow p_z$), despite the fact that the two sides of this equation are not adiabatically deformable into one other [51, 54].

The natural next step is to derive the dominant interaction terms in the problem by connecting our model to the micro-

scopic degrees of freedom in TBG. Ideally, we would like to isolate the relevant bands in the continuum model and construct Wannier states which correspond to our tight-binding orbitals. We caution, however, that band crossings may occur at higher energies, so that isolating the relevant bands may require some judgement, although we do not expect this to affect the low energy physics.

Another interesting future direction is to study how the unconventional nature of fragile topology might inform the physics of the interaction problem. Since the complementary trivial bands are fully filled, they correspond to an atomic insulator. In the limit where the band gap is much larger than the interaction strength, the problem should reduce to one involving certain local constraints on the Hilbert space, which has not previously been explored in this context. We leave these questions for future work.

Note added: In finalizing this manuscript, Ref. 55 appeared, which proposes a four-band (per valley and per spin) tight-binding model similar to that described in Ref. 29. They

also suggest that the band topology in TBG is stable rather than fragile, based on the properties of Wilson loops [56]. As shown in Appendix D, the nearly flat bands in our tight-binding models have the same nontrivial Wilson loop invariant as identified in Ref. 55. However, we have explicitly demonstrated that their band topology is fragile. As stable and fragile topologies are mutually exclusive, this implies the known forms of band topology in TBG cannot be stable.

ACKNOWLEDGMENTS

We thank S. Fang, E. Kaxiras, and M. Zaletel for helpful discussions. TS is supported by a US Department of Energy grant DE-SC0008739, and in part by a Simons Investigator award from the Simons Foundation. AV was supported by a Simons Investigator award and by NSF-DMR 1411343.

-
- [1] P. A. Lee, N. Nagaosa, and X.-G. Wen, *Rev. Mod. Phys.* **78**, 17 (2006).
- [2] Y. Cao, V. Fatemi, A. Demir, S. Fang, S. L. Tomarken, J. Y. Luo, J. D. Sanchez-Yamagishi, K. Watanabe, T. Taniguchi, E. Kaxiras, R. C. Ashoori, and P. Jarillo-Herrero, *Nature*, EP (2018).
- [3] Y. Cao, V. Fatemi, S. Fang, K. Watanabe, T. Taniguchi, E. Kaxiras, and P. Jarillo-Herrero, *Nature*, EP (2018).
- [4] J. M. B. Lopes dos Santos, N. M. R. Peres, and A. H. Castro Neto, *Phys. Rev. Lett.* **99**, 256802 (2007).
- [5] G. Li, A. Luican, J. M. B. Lopes dos Santos, A. H. Castro Neto, A. Reina, J. Kong, and E. Y. Andrei, *Nature Physics* **6**, 109 EP (2009).
- [6] G. Trambly de Laissardière, D. Mayou, and L. Magaud, *Nano Letters*, *Nano Letters* **10**, 804 (2010).
- [7] E. J. Mele, *Phys. Rev. B* **81**, 161405 (2010).
- [8] S. Shallcross, S. Sharma, E. Kandelaki, and O. A. Pankratov, *Phys. Rev. B* **81**, 165105 (2010).
- [9] R. Bistritzer and A. H. MacDonald, *Phys. Rev. B* **81**, 245412 (2010).
- [10] E. Suárez Morell, J. D. Correa, P. Vargas, M. Pacheco, and Z. Barticevic, *Phys. Rev. B* **82**, 121407 (2010).
- [11] A. Luican, G. Li, A. Reina, J. Kong, R. R. Nair, K. S. Novoselov, A. K. Geim, and E. Y. Andrei, *Phys. Rev. Lett.* **106**, 126802 (2011).
- [12] R. Bistritzer and A. H. MacDonald, *Proceedings of the National Academy of Sciences* **108**, 12233 (2011), <http://www.pnas.org/content/108/30/12233.full.pdf>.
- [13] R. de Gail, M. O. Goerbig, F. Guinea, G. Montambaux, and A. H. Castro Neto, *Phys. Rev. B* **84**, 045436 (2011).
- [14] J. M. B. Lopes dos Santos, N. M. R. Peres, and A. H. Castro Neto, *Phys. Rev. B* **86**, 155449 (2012).
- [15] W.-Y. He, Z.-D. Chu, and L. He, *Phys. Rev. Lett.* **111**, 066803 (2013).
- [16] K. Uchida, S. Furuya, J.-I. Iwata, and A. Oshiyama, *Phys. Rev. B* **90**, 155451 (2014).
- [17] W. Yan, M. Liu, R.-F. Dou, L. Meng, L. Feng, Z.-D. Chu, Y. Zhang, Z. Liu, J.-C. Nie, and L. He, *Phys. Rev. Lett.* **109**, 126801 (2012).
- [18] J. Jung, A. Raoux, Z. Qiao, and A. H. MacDonald, *Phys. Rev. B* **89**, 205414 (2014).
- [19] A. O. Sboychakov, A. L. Rakhmanov, A. V. Rozhkov, and F. Nori, *Phys. Rev. B* **92**, 075402 (2015).
- [20] D. Wong, Y. Wang, J. Jung, S. Pezzini, A. M. DaSilva, H.-Z. Tsai, H. S. Jung, R. Khajeh, Y. Kim, J. Lee, S. Kahn, S. Tolabimazraehno, H. Rasool, K. Watanabe, T. Taniguchi, A. Zettl, S. Adam, A. H. MacDonald, and M. F. Crommie, *Phys. Rev. B* **92**, 155409 (2015).
- [21] S. Fang and E. Kaxiras, *Phys. Rev. B* **93**, 235153 (2016).
- [22] Y. Cao, J. Y. Luo, V. Fatemi, S. Fang, J. D. Sanchez-Yamagishi, K. Watanabe, T. Taniguchi, E. Kaxiras, and P. Jarillo-Herrero, *Phys. Rev. Lett.* **117**, 116804 (2016).
- [23] K. Kim, A. DaSilva, S. Huang, B. Fallahzad, S. Larentis, T. Taniguchi, K. Watanabe, B. J. LeRoy, A. H. MacDonald, and E. Tutuc, *Proceedings of the National Academy of Sciences* **114**, 3364 (2017).
- [24] N. N. T. Nam and M. Koshino, *Phys. Rev. B* **96**, 075311 (2017).
- [25] S. Huang, K. Kim, D. K. Efimkin, T. Lovorn, T. Taniguchi, K. Watanabe, A. H. MacDonald, E. Tutuc, and B. J. LeRoy, ArXiv e-prints (2018), [arXiv:1802.02999](https://arxiv.org/abs/1802.02999).
- [26] P. Rickhaus, J. Wallbank, S. Slizovskiy, R. Pisoni, H. Overweg, Y. Lee, M. Eich, M.-H. Liu, K. Watanabe, T. Taniguchi, V. Fal'ko, T. Ihn, and K. Ensslin, ArXiv e-prints (2018), [arXiv:1802.07317](https://arxiv.org/abs/1802.07317).
- [27] A. Ramires and J. L. Lado, ArXiv e-prints (2018), [arXiv:1803.04400](https://arxiv.org/abs/1803.04400).
- [28] H. C. Po, L. Zou, A. Vishwanath, and T. Senthil, ArXiv e-prints (2018), [arXiv:1803.09742](https://arxiv.org/abs/1803.09742).
- [29] L. Zou, H. C. Po, A. Vishwanath, and T. Senthil, ArXiv e-prints (2018), [arXiv:1806.07873](https://arxiv.org/abs/1806.07873).
- [30] M. Goerbig and G. Montambaux, "Dirac fermions in condensed matter and beyond," in *Dirac Matter*, edited by B. Duplantier, V. Rivasseau, and J.-N. Fuchs (Springer International Publishing, Cham, 2017) pp. 25–53.
- [31] H. Matsumoto, M. Sasaki, and M. Tachiki, *Solid State Communications* **71**, 829 (1989).
- [32] F. D. M. Haldane, *Phys. Rev. Lett.* **61**, 2015 (1988).
- [33] C. L. Kane and E. J. Mele, *Phys. Rev. Lett.* **95**, 146802 (2005).
- [34] C. L. Kane and E. J. Mele, *Phys. Rev. Lett.* **95**, 226801 (2005).

- [35] A. Kitaev, *AIP Conference Proceedings* **1134**, 22 (2009).
- [36] D. S. Freed and G. W. Moore, *Annales Henri Poincaré* **14**, 1927 (2013).
- [37] J. C. Y. Teo and C. L. Kane, *Phys. Rev. B* **82**, 115120 (2010).
- [38] H. C. Po, H. Watanabe, and A. Vishwanath, ArXiv e-prints (2017), [arXiv:1709.06551](#).
- [39] N. F. Q. Yuan and L. Fu, ArXiv e-prints (2018), [arXiv:1803.09699](#).
- [40] J. Kang and O. Vafek, ArXiv e-prints (2018), [arXiv:1805.04918](#).
- [41] M. Koshino, N. F. Q. Yuan, M. Ochi, K. Kuroki, and L. Fu, ArXiv e-prints (2018), [arXiv:1805.06819](#).
- [42] C. Xu and L. Balents, ArXiv e-prints (2018), [arXiv:1803.08057](#).
- [43] J. F. Dodaro, S. A. Kivelson, Y. Schattner, X.-Q. Sun, and C. Wang, (2018), [arXiv:1804.03162](#).
- [44] L. Zhang, (2018), [arXiv:1804.09047](#).
- [45] L. Rademaker and P. Mellado, (2018), [arXiv:1805.05294](#).
- [46] A. Thomson, S. Chatterjee, S. Sachdev, and M. S. Scheurer, (2018), [arXiv:1806.02837](#).
- [47] E. H. Lieb, *Phys. Rev. Lett.* **62**, 1201 (1989).
- [48] A. A. Soluyanov and D. Vanderbilt, *Phys. Rev. B* **83**, 035108 (2011).
- [49] H. C. Po, H. Watanabe, M. P. Zaletel, and A. Vishwanath, *Sci. Adv.* **2** (2016).
- [50] H. C. Po, A. Vishwanath, and H. Watanabe, *Nature Communications* **8**, 50 (2017).
- [51] B. Bradlyn, L. Elcoro, J. Cano, M. G. Vergniory, Z. Wang, C. Felser, M. I. Aroyo, and B. A. Bernevig, *Nature* **547**, 298 EP (2017), article.
- [52] J. Cano, B. Bradlyn, Z. Wang, L. Elcoro, M. G. Vergniory, C. Felser, M. I. Aroyo, and B. A. Bernevig, *Phys. Rev. Lett.* **120**, 266401 (2018).
- [53] A. Bouhon, A. M. Black-Schaffer, and R.-J. Slager, (2018), [arXiv:1804.09719](#).
- [54] L. Michel and J. Zak, *Phys. Rep.* **341**, 377 (2001).
- [55] Z. Song, Z. Wang, W. Shi, G. Li, C. Fang, and B. A. Bernevig, ArXiv e-prints (2018), [arXiv:1807.10676](#).
- [56] A. Alexandradinata, Z. Wang, and B. A. Bernevig, *Phys. Rev. X* **6**, 021008 (2016).

Appendix A: Symmetry representations

In this appendix, we providing some details regarding the symmetry representations in the problem. In Table III we provide the symmetry properties of the fermion operators. Note that we have included a time-reversal-like operation \tilde{T} , which is *not* a symmetry of the problem, but is considered for simplifying our discussion.

TABLE III. Action of symmetries on the real-space orbitals. Given a symmetry g and the fermion creation operator \hat{c}^\dagger for an orbital, we tabulate the outcome of $\hat{g}\hat{c}^\dagger\hat{g}^{-1}$. Note that the action of anti-unitary operators is ambiguous up to an arbitrarily choice on $U(1)$ phases. Also, the time-reversal-like symmetry \tilde{T} is *not* a symmetry of our problem, as the actual time-reversal symmetry of twisted bilayer graphene exchanges the two valleys. We include \tilde{T} here merely to simplify the discussion, and it would be broken explicitly. We let $\omega \equiv e^{i2\pi/3}$.

| g | \hat{s}^\dagger | \hat{p}_z^\dagger | \hat{p}_+^\dagger | \hat{p}_-^\dagger |
|------------------|-------------------|----------------------|---------------------------|-----------------------------|
| C_3 | \hat{s}^\dagger | \hat{p}_z^\dagger | $\omega\hat{p}_+^\dagger$ | $\omega^*\hat{p}_-^\dagger$ |
| M_y | \hat{s}^\dagger | $-\hat{p}_z^\dagger$ | \hat{p}_-^\dagger | \hat{p}_+^\dagger |
| $C_2\mathcal{T}$ | \hat{s}^\dagger | \hat{p}_z^\dagger | \hat{p}_-^\dagger | \hat{p}_+^\dagger |
| \tilde{T} | \hat{s}^\dagger | \hat{p}_z^\dagger | $-\hat{p}_-^\dagger$ | $-\hat{p}_+^\dagger$ |

In Table IV, we provide the momentum-space representations arising from the full-filling of orbitals in real-space, i.e., atomic insulators. The real-space orbitals we will consider include: (τ, s) , (τ, p_z) , (τ, p_\pm) , (η, s) , (η, p_z) , (η, p_\pm) , (κ, s) and (κ, p_z) . Notice that when a pair of states at Γ have C_3 representation of (ω, ω^*) , these two states must have M_y eigenvalues $(+1, -1)$. In other words, these two states form the two dimensional representation of symmetry $D_3 \simeq \langle C_3 \rangle \times \langle M_y \rangle$, where $\langle g \rangle$ indicates the subgroup generated by the element g .

TABLE IV. The resulting symmetry representations at high-symmetry points from various real-space orbitals. Eigenvalues from degenerate bands are grouped by parenthesis. Note that M_y is not a symmetry at K.

| (τ, s) | Γ | K | (τ, p_z) | Γ | K | (τ, p_\pm) | Γ | K |
|-------------|----------|---|---------------|----------|---|-----------------|----------------------|----------------------|
| C_3 | 1 | 1 | C_3 | 1 | 1 | C_3 | (ω, ω^*) | (ω, ω^*) |
| M_y | 1 | | M_y | -1 | | M_y | $(1, -1)$ | |

| (η, s) | Γ | K | (η, p_z) | Γ | K | (η, p_\pm) | Γ | K |
|-------------|----------|----------------------|---------------|----------|----------------------|-----------------|--|----------------------------|
| C_3 | 1, 1 | (ω, ω^*) | C_3 | 1, 1 | (ω, ω^*) | C_3 | $(\omega, \omega^*), (\omega, \omega^*)$ | 1, 1, (ω, ω^*) |
| M_y | 1, 1 | | M_y | -1, -1 | | M_y | $(1, -1), (1, -1)$ | |

| (κ, s) | Γ | K | (κ, p_z) | Γ | K |
|---------------|-------------------------|-------------------------|-----------------|-------------------------|-------------------------|
| C_3 | 1, (ω, ω^*) | 1, (ω, ω^*) | C_3 | 1, (ω, ω^*) | 1, (ω, ω^*) |
| M_y | 1, $(1, -1)$ | | M_y | -1, $(1, -1)$ | |

From Table IV, one can find all possible representation-matching equations that can be used to resolve the Wannier obstruction in a “fragile” manner. (Alternatively, one could have also resolved it by appending topological bands, as we discussed in Ref. 29.) For example, there are two representation-matching equations involving only three bands:

$$\begin{aligned}
(\tau, s) \oplus (\eta, p_z) &\stackrel{\text{rep.}}{=} (\tau, p_z) \oplus (\text{target}); \\
(\tau, p_z) \oplus (\eta, s) &\stackrel{\text{rep.}}{=} (\tau, s) \oplus (\text{target}).
\end{aligned} \tag{A1}$$

This is the minimal number of bands that are needed to resolve the obstruction in terms of representations, although we did not find a suitable set of parameters for realizing this. Building from these two representation-matching equations, one can add trivial bands on both sides of the equation and get a new equation. We will call the latter a derived equation from the former.

When the number of bands involved is four, the representation-matching equations that can potentially lead to a resolution of the obstruction are all derived equations of the above ones. With five bands, however, there are new representation-matching

equations:

$$\begin{aligned} (\eta, p_z) \oplus (\kappa, s) &\stackrel{\text{rep.}}{\equiv} (\kappa, p_z) \oplus (\text{target}); \\ (\eta, s) \oplus (\kappa, p_z) &\stackrel{\text{rep.}}{\equiv} (\kappa, s) \oplus (\text{target}). \end{aligned} \quad (\text{A2})$$

From these equations and using

$$\begin{aligned} (\tau, s) \oplus (\tau, p_{\pm}) &\stackrel{\text{rep.}}{\equiv} (\kappa, s); \\ (\tau, p_z) \oplus (\tau, p_{\pm}) &\stackrel{\text{rep.}}{\equiv} (\kappa, p_z), \end{aligned} \quad (\text{A3})$$

one obtains

$$\begin{aligned} (\eta, p_z) \oplus (\tau, s) \oplus (\tau, p_{\pm}) &\stackrel{\text{rep.}}{\equiv} (\kappa, p_z) \oplus (\text{target}) \stackrel{\text{rep.}}{\equiv} (\tau, p_z) \oplus (\tau, p_{\pm}) \oplus (\text{target}); \\ (\eta, s) \oplus (\tau, p_z) \oplus (\tau, p_{\pm}) &\stackrel{\text{rep.}}{\equiv} (\kappa, s) \oplus (\text{target}) \stackrel{\text{rep.}}{\equiv} (\tau, s) \oplus (\tau, p_{\pm}) \oplus (\text{target}). \end{aligned} \quad (\text{A4})$$

When there are six bands, there are also new representation-matching equations that are not derived ones of equations with fewer bands:

$$\begin{aligned} (\tau, p_z) \oplus (\tau, p_{\pm}) \oplus (\kappa, s) &\stackrel{\text{rep.}}{\equiv} (\eta, p_{\pm}) \oplus (\text{target}); \\ (\tau, s) \oplus (\tau, p_{\pm}) \oplus (\kappa, p_z) &\stackrel{\text{rep.}}{\equiv} (\eta, p_{\pm}) \oplus (\text{target}), \end{aligned} \quad (\text{A5})$$

where the first one is precisely Eq. (1) used in the main text. From these equations and using Eq. (A3), one can obtain other equations:

$$\begin{aligned} (\tau, s) \oplus (\tau, p_z) \oplus (\tau, p_{\pm}) \oplus (\tau, p_{\pm}) &\stackrel{\text{rep.}}{\equiv} (\eta, p_{\pm}) \oplus (\text{target}); \\ (\kappa, p_z) \oplus (\kappa, s) &\stackrel{\text{rep.}}{\equiv} (\eta, p_{\pm}) \oplus (\text{target}). \end{aligned} \quad (\text{A6})$$

Up to six bands, it is straightforward to check that the above are all the independent representation-matching equations that can potentially lead to a fragile resolution of the Wannier obstructions. Here, by ‘‘independent’’ we mean that these equations cannot be viewed as a derived one from another.

Appendix B: Details of the Bloch Hamiltonian

In this appendix, we provide further details on the Bloch Hamiltonians constructed in this work. In particular, we provide the explicit expression for the Hamiltonians. Unlike the presentation in the main text, we find it more natural to first discuss the six-band model, and then move on to the ten-band one.

1. Six-band model

Here, we document explicitly the symmetry-allowed terms entering into the six-band model we constructed. In the following, all the coupling parameters t are real numbers.

Recall our six-band Hilbert space arises from (τ, p_z) , (τ, p_{\pm}) , and (κ, s) . Let us write the fermion operator for orbitals in the unit cell \mathbf{r} as

$$\hat{\mathbf{c}}_{\mathbf{r}}^{\dagger} \equiv \left(\hat{\tau}_{p_z; \mathbf{r}}^{\dagger} \quad \hat{\tau}_{p_+; \mathbf{r}}^{\dagger} \quad \hat{\tau}_{p_-; \mathbf{r}}^{\dagger} \quad \hat{\kappa}_{s; \mathbf{r}}^{(1)\dagger} \quad \hat{\kappa}_{s; \mathbf{r}}^{(2)\dagger} \quad \hat{\kappa}_{s; \mathbf{r}}^{(3)\dagger} \right), \quad (\text{B1})$$

which fixes our basis choice of the Bloch Hamiltonian.

As discussed in the main text, the terms in our six-band Hamiltonian will mostly be conventional nearest-neighbor bonds, with the sole exception of a second nearest-neighbor bond included for (κ, s) . Let us discuss these terms one-by-one. First, the nearest-neighbor bond between the (τ, p_z) orbitals takes the standard form on the triangular lattice:

$$H_{p_z} = t_{p_z} (\phi_{01} + \phi_{11} + \phi_{10} + \text{h.c.}), \quad (\text{B2})$$

where we let $\phi_{lm} = e^{-i\mathbf{k} \cdot (l\mathbf{a}_1 + m\mathbf{a}_2)}$, and we denote negative numbers by $\bar{l} \equiv -l$.

The nearest-neighbor couplings for the (τ, p_{\pm}) orbitals are slightly more complicated due to the two-orbital structure. First, the intra-orbital piece is identical to H_{p_z} , but with $t_{p_z} \mapsto t_{p_{\pm}}$ and multiplied by the 2×2 identity matrix. Second, there is also an inter-orbital coupling, which in momentum-space is given by

$$\mathcal{C}_{p_{\pm}p_{\pm}} = t_{p_{\pm}p_{\pm}}^+ (\phi_{01} + \phi_{\bar{1}\bar{1}}\omega + \phi_{10}\omega^*) + t_{p_{\pm}p_{\pm}}^- (\phi_{0\bar{1}} + \phi_{11}\omega + \phi_{\bar{1}0}\omega^*), \quad (\text{B3})$$

where $\omega = e^{i2\pi/3}$. This gives the Bloch Hamiltonian

$$H_{p_{\pm}} = t_{p_{\pm}} (\phi_{01} + \phi_{11} + \phi_{10} + \text{h.c.}) \begin{pmatrix} 1 & 0 \\ 0 & 1 \end{pmatrix} + \begin{pmatrix} 0 & \mathcal{C}_{p_{\pm}p_{\pm}}^{\dagger} \\ \mathcal{C}_{p_{\pm}p_{\pm}} & 0 \end{pmatrix}. \quad (\text{B4})$$

Next, we consider the kagome lattice. Aside from the standard nearest-neighbor bond t_{κ} , we find it natural to also incorporate the second nearest-neighbor bond t'_{κ} , for otherwise there would be an artificial (almost) flat band in the spectrum. This gives

$$H_{\kappa} = t_{\kappa} \begin{pmatrix} 0 & \phi_{\bar{1}0} & 1 \\ 1 & 0 & \phi_{0\bar{1}} \\ \phi_{11} & 1 & 0 \end{pmatrix} + t'_{\kappa} \begin{pmatrix} 0 & \phi_{\bar{1}\bar{1}} & \phi_{\bar{1}0} \\ \phi_{0\bar{1}} & 0 & \phi_{10} \\ \phi_{01} & \phi_{11} & 0 \end{pmatrix} + \text{h.c.} \quad (\text{B5})$$

Lastly, we consider the nearest-neighbor coupling between the different lattices. In momentum space they are characterized by

$$\begin{aligned} \mathcal{C}_{p_{\pm}p_z} &= it_{p_{\pm}p_z}^+ \begin{pmatrix} \phi_{01} + \phi_{\bar{1}\bar{1}}\omega + \phi_{10}\omega^* \\ -(\phi_{0\bar{1}} + \phi_{11}\omega^* + \phi_{\bar{1}0}\omega) \end{pmatrix} - it_{p_{\pm}p_z}^- \begin{pmatrix} \phi_{0\bar{1}} + \phi_{11}\omega + \phi_{\bar{1}0}\omega^* \\ -(\phi_{01} + \phi_{\bar{1}\bar{1}}\omega^* + \phi_{10}\omega) \end{pmatrix}; \\ \mathcal{C}_{\kappa p_{\pm}} &= t_{\kappa p_{\pm}}^+ \begin{pmatrix} \phi_{\bar{1}0} & \phi_{\bar{1}\bar{1}} \\ \phi_{\bar{1}\bar{1}}\omega^* & \omega \end{pmatrix} - t_{\kappa p_{\pm}}^- \begin{pmatrix} \phi_{\bar{1}\bar{1}} & \phi_{\bar{1}0} \\ \omega^* & \phi_{\bar{1}\bar{1}}\omega \end{pmatrix}. \end{aligned} \quad (\text{B6})$$

Here, the subscript $p_{\pm}p_z$ indicates coupling between the (τ, p_{\pm}) and the (τ, p_z) orbitals, and κp_{\pm} indicates that between (κ, s) and (τ, p_{\pm}) . The real-space form of all the nontrivial couplings above is represented diagrammatically in Fig. 5.

Altogether, the full Bloch Hamiltonian of the six-band model is given by

$$H^{(6)} = \begin{pmatrix} H_{p_z} + \mu_{p_z} & \mathcal{C}_{p_{\pm}p_z}^{\dagger} & 0 \\ \mathcal{C}_{p_{\pm}p_z} & H_{p_{\pm}} + \mu_{p_{\pm}} & \mathcal{C}_{\kappa p_{\pm}}^{\dagger} \\ 0 & \mathcal{C}_{\kappa p_{\pm}} & H_{\kappa} + \mu_{\kappa} \end{pmatrix} \quad (\text{B7})$$

where we have added relative chemical potentials μ_i across the different lattices. For reasons that will become clearer later, we find it convenient to reparameterize these parameters as

$$\mu_{p_z} \equiv -6t_{p_z} + \delta_{p_z}; \quad \mu_{p_{\pm}} \equiv 3t_{p_{\pm}} + \delta_{p_{\pm}}; \quad \& \quad \mu_{\kappa} \equiv -4(t_{\kappa} + t'_{\kappa}) + \delta_{\kappa}. \quad (\text{B8})$$

Before we proceed, we make two remarks regarding the model parameters. First, note that we have ignored the coupling between the (τ, p_z) and (κ, s) orbitals, as we find its inclusion to be unnecessary for reproducing the key energetic features of the dispersion. In practice, such terms are symmetry-allowed and would never be exactly zero, but since we only address symmetry-robust features in the problem their presence has little physical implications. As such, we choose to keep it at 0 to simplify the discussion.

Second, we have parameterized the coupling strengths such that when $t_{p_{\pm}p_z}^+ - t_{p_{\pm}p_z}^- = t_{p_z}^+ - t_{p_z}^- = t_{\kappa p_{\pm}}^+ - t_{\kappa p_{\pm}}^- = 0$, $H^{(6)}$ will be $\tilde{\mathcal{T}}$ -invariant. Since the time-reversal-like operation $\tilde{\mathcal{T}}$ is not an actual symmetry of the problem, this relation will not hold in our model parameters. This parameterization is nonetheless adopted as it provides a simple way to control the degree of $\tilde{\mathcal{T}}$ -breaking in the spectrum.

Next, we expand on the discussion in the main text concerning a physical picture for our model parameters. Recall that the electronic weights of TBG sit mostly at the AA spots, which form a triangular lattice at the moiré scale [5, 6, 11, 16, 20–22]. In addition, the Dirac points at K and K' are naturally explained by the symmetry characters of the (τ, p_{\pm}) orbitals. The main nontrivial feature of the nearly flat bands, therefore, stems from the fact that at Γ points the non-degenerate bands *cannot* come from the (τ, p_{\pm}) orbitals due to a mismatch in the symmetry representations. Rather, in our Hilbert space they can only arise from the (τ, p_z) and (κ, s) orbitals. Our goal is to choose parameters such that the orbital characters of the nearly flat bands behave as expected across the entire Brillouin zone (BZ).

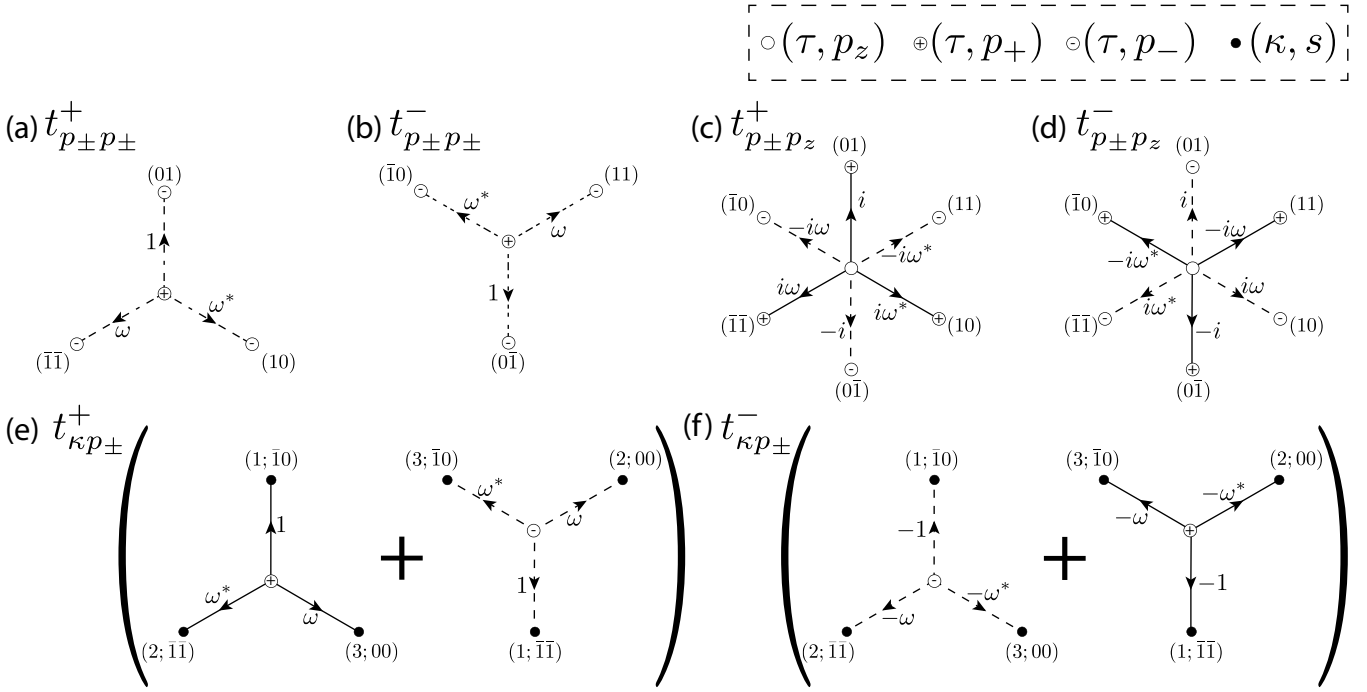


FIG. 5. Coupling terms in the six-band model. The full coupling terms consist of the indicated hopping together with their Hermitian conjugates. We always take the center site to be a triangular site in the “home” unit cell, and indicate the unit cell coordinates of connected sites by (lm) with $\bar{l} \equiv -l$. For the kagome sites in (e,f), we further specify their sublattice indices. The strength of the terms in panels (a-f) are respectively denoted by $t_{p_{\pm}p_{\pm}}^+$, $t_{p_{\pm}p_{\pm}}^-$, $t_{p_{\pm}p_z}^+$, $t_{p_{\pm}p_z}^-$, $t_{\kappa p_{\pm}}^+$, and $t_{\kappa p_{\pm}}^-$.

First, let us ignore all the nontrivial coupling terms by setting $t_{p_{\pm}p_{\pm}}^{\pm} = t_{p_{\pm}p_z}^{\pm} = t_{\kappa p_{\pm}}^{\pm} = 0$. As discussed, the nearly flat bands will be formed by the (τ, p_z) and (κ, s) orbitals at Γ , and the (τ, p_{\pm}) Dirac points at K and K' . In our parameterization, we can arrange all these orbitals to be at zero-energy by setting $\delta_{p_z} = \delta_{p_{\pm}} = \delta_{\kappa} = 0$. Furthermore, by adjusting the values of δ_{p_z} and δ_{κ} we can set the bandwidth of the nearly flat bands.

As the wave functions of the nearly flat bands at Γ must arise from the (τ, p_z) and (κ, s) orbitals, we should bring down the energy of the (τ, p_{\pm}) bands at Γ . This is achieved by choosing $t_{p_{\pm}} < 0$. This sets up the required orbital characters for the bands near zero energy: (τ, p_z) and (κ, s) at Γ but (τ, p_{\pm}) in the rest of the BZ. We are then left with the (τ, p_z) and (κ, s) bands at most of the BZ, as well as the (τ, p_{\pm}) -Dirac point at Γ . Observe that the bandwidth of the four connected bands below the nearly flat bands set the dominant energy scale in the band manifold we intend to describe. This bandwidth can be reconciled with the size of t_{κ} , and therefore we choose it to be the reference energy scale and measure all the other terms with respect to it. We also choose the values of t_{p_z} and t'_{κ} to reproduce the broad energetic features of the bands.

Fig. 3b in the main text shows the band dispersion we obtained following the discussion above. Observe that the broad energetic features are already in place. It remains to turn on the nontrivial couplings between the orbitals, and open band gaps to isolate the two nearly flat bands at the top. Our chosen parameters are tabulated in Table V, and the corresponding band structure is shown in Fig. 3c in the main text. Note that some parameters are roughly an order of magnitude smaller than the others; they are adjusted to capture the fine energetic features in the nearly flat bands.

2. Ten-band model

Next, we discuss the terms in the ten-band model. Here, the dominant energetic features are imprinted by the choice of the “quasi-orbital” fermion operator $\hat{h}_{p_{\pm};r}^{(l)\dagger} \equiv \sum_{\mathbf{x}} \hat{c}_{\mathbf{x}}^{\dagger} h_{p_{\pm};r}^{(l)}(\mathbf{x})$. We have already provided the explicit form of the localized wave functions $h_{p_{\pm};r}^{(l)}(\mathbf{x})$ in real space in Fig. 1b of the main text. However, it will be convenient to also write down explicitly the

TABLE V. Hopping parameters in the six-band model. We abbreviate “nearest neighbor” to “nnbr.” We set the dominant energy scale to be $t_\kappa = 27$ meV, and measure all the other terms relative to that.

| Parameter | Meaning | Ratio to t_κ |
|---|--------------------------------------|---------------------|
| $\delta_{p_z} \equiv \mu_{p_z} + 6t_{p_z}$ | (τ, p_z) chemical potential | 0 |
| $\delta_{p_\pm} \equiv \mu_{p_\pm} - 3t_{p_\pm}$ | (τ, p_\pm) chemical potential | -0.23 |
| $\delta_\kappa \equiv \mu_\kappa + 4(t_\kappa + t'_\kappa)$ | (κ, s) chemical potential | 0.25 |
| t_{p_z} | (τ, p_z) nnbr | 0.17 |
| t_{p_\pm} | (τ, p_\pm) intra-orbital nnbr | -0.017 |
| $t_{p_\pm p_\pm}^+$ | (τ, p_\pm) inter-orbital nnbr | -0.065 |
| $t_{p_\pm p_\pm}^-$ | (τ, p_\pm) inter-orbital nnbr | -0.055 |
| t_κ | (κ, s) nnbr | 1 |
| t'_κ | (κ, s) second-nnbr | 0.25 |
| $t_{p_\pm p_z}^+$ | (τ, p_\pm) - (τ, p_z) nnbr | 0.095 |
| $t_{p_\pm p_z}^-$ | (τ, p_\pm) - (τ, p_z) nnbr | 0.055 |
| $t_{\kappa p_\pm}^+$ | (κ, s) - (τ, p_\pm) nnbr | 0.6 |
| $t_{\kappa p_\pm}^-$ | (κ, s) - (τ, p_\pm) nnbr | 0.2 |

Fourier transform of these wave function in momentum space:

$$\begin{aligned}
 h_{p_+; \mathbf{k}}^{(A)} &= \begin{pmatrix} -(\omega + \phi_{11}\omega^* + \phi_{01})\zeta^* a \\ (\omega^* + \phi_{11}\omega + \phi_{01})\zeta b \\ (1 + \phi_{11} + \phi_{01})c \\ -i\phi_{\bar{1}0}d \\ -i\omega d \\ -i\phi_{01}\omega^* d \end{pmatrix}; \quad h_{p_-; \mathbf{k}}^{(A)} = \begin{pmatrix} (1 + \phi_{11}\omega^* + \phi_{01}\omega)\zeta^* a \\ (1 + \phi_{11} + \phi_{01})c \\ (1 + \omega\phi_{11} + \omega^*\phi_{01})\zeta b \\ -i\phi_{\bar{1}0}d \\ -i\omega^* d \\ -i\phi_{01}\omega d \end{pmatrix}; \\
 h_{p_+; \mathbf{k}}^{(B)} &= \begin{pmatrix} (\omega + \phi_{10}\omega^* + \phi_{11})\zeta a \\ (\omega^* + \phi_{10}\omega + \phi_{11})\zeta^* b \\ (1 + \phi_{10} + \phi_{11})c \\ id \\ i\omega d \\ i\omega^* d \end{pmatrix}; \quad h_{p_-; \mathbf{k}}^{(B)} = \begin{pmatrix} -(\omega + \phi_{10} + \phi_{11}\omega^*)\zeta a \\ (1 + \phi_{10} + \phi_{11})c \\ (\omega^* + \phi_{10} + \phi_{11}\omega)\zeta^* b \\ id \\ i\omega^* d \\ i\omega d \end{pmatrix}.
 \end{aligned} \tag{B9}$$

Furthermore, it is natural to group these four column vectors into a single 6×4 matrix:

$$h_{\mathbf{k}} = \begin{pmatrix} h_{p_+; \mathbf{k}}^{(A)} & h_{p_-; \mathbf{k}}^{(A)} & h_{p_+; \mathbf{k}}^{(B)} & h_{p_-; \mathbf{k}}^{(B)} \end{pmatrix}. \tag{B10}$$

The Bloch Hamiltonian corresponding to Eq. (3) with $\delta = 0$ can then be written as

$$H_{\mathbf{k}}(t, 0) = t \begin{pmatrix} 0_{6 \times 6} & h_{\mathbf{k}} \\ h_{\mathbf{k}}^\dagger & 0_{4 \times 4} \end{pmatrix}. \tag{B11}$$

Note the block structure of $H(t, 0)$; we see immediately that $H(t, 0)$ anti-commutes with $\mathbb{1}_{6 \times 6} \oplus (-\mathbb{1}_{4 \times 4})$, implying $H_{\mathbf{k}}(t, 0)$ will be particle-hole symmetric at every \mathbf{k} . Also, as $h_{\mathbf{k}}^\dagger$ is a 4×6 rectangular matrix, the equation

$$h_{\mathbf{k}}^\dagger \varphi = 0 \tag{B12}$$

must have at least two non-trivial solutions at every \mathbf{k} . In other words, there will be (at least) two exactly flat bands at zero-energy in the spectrum of $H(t, 0)$ (Fig. 2a and d in the main text). For generic choices of the parameters $a-d$, these will be the only states at zero-energy, and they serve as the precursor for the nearly flat bands in the final model.

TABLE VI. Hopping parameters in the ten-band model. We abbreviate “nearest neighbor” to “nnbr.” We measure the strengths of the various terms relative to the dominate one, $t_\eta = 32.5$ meV. All terms present in Table V but not here are set to 0.

| Parameter | Meaning | Ratio to t_η |
|---|--------------------------------------|-------------------|
| $\delta_{p_z} \equiv \mu_{p_z} + 6t_{p_z}$ | (τ, p_z) chemical potential | -0.100 |
| $\delta_\kappa \equiv \mu_\kappa + 4(t_\kappa + t'_\kappa)$ | (κ, s) chemical potential | 0.110 |
| t_{p_z} | (τ, p_z) nnbr | 0 |
| t_{p_\pm} | (τ, p_\pm) intra-orbital nnbr | 0.003 |
| $t_{p_\pm p_\pm}^-$ | (τ, p_\pm) inter-orbital nnbr | 0.004 |
| t_κ | (κ, s) nnbr | 0 |
| t'_κ | (κ, s) second-nnbr | 0 |
| $t_{p_\pm p_z}^+$ | (τ, p_\pm) - (τ, p_z) nnbr | 0.016 |
| $t_{\kappa p_\pm}^+$ | (κ, s) - (τ, p_\pm) nnbr | 0.016 |
| $t_{\kappa p_\pm}^-$ | (κ, s) - (τ, p_\pm) nnbr | -0.016 |
| $t_\eta e^{i\phi_\eta}$ | (η, p_\pm) nnbr | i |

Our next step is to add generic perturbations to reproduce the actual energetic features of the TBG spectrum. There are two main features which we wish to capture: (i) the dispersion of the nearly flat bands; and (ii) the absence of \tilde{T} in the higher-energy bands. For (i), we simply add a subset of the terms we used in constructing the six-band model. For (ii), we consider an additional nearest-neighbor coupling between the (η, p_\pm) orbitals, which are present only in the ten-band Hilbert space. As in the previous discussion, we represent the term diagrammatically in Fig. 6, and provide the explicit expression:

$$H_\eta = t_\eta \begin{pmatrix} 0 & e^{i\phi_\eta}(1 + \phi_{0\bar{1}} + \phi_{10}) \\ e^{-i\phi_\eta}(1 + \phi_{01} + \phi_{\bar{1}0}) & 0 \end{pmatrix} \otimes \mathbb{1}_{2 \times 2}, \quad (\text{B13})$$

where t_η, ϕ_η are real parameters. In order to break the undesirable \tilde{T} -invariance, we will choose $\phi_\eta \neq 0, \pi$.

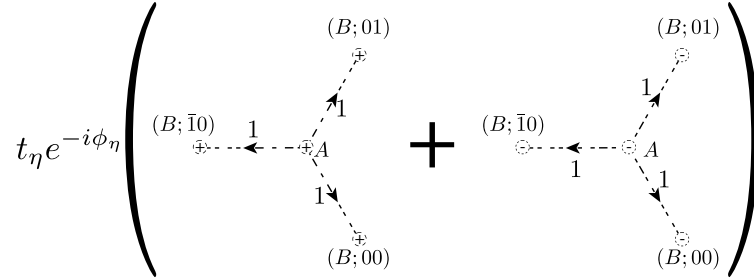


FIG. 6. The leading perturbation to the ten-band model, which breaks the undesirable \tilde{T} -invariance. Each circle denotes a honeycomb site, with the orbital p_\pm indicated.

Altogether, the perturbation to the ten-band model is, in a block-matrix form, given by

$$V_{\mathbf{k}} = \begin{pmatrix} \mu_{p_z} & C_{p_\pm p_z}^\dagger & 0 & 0 \\ C_{p_\pm p_z} & H_{p_\pm} + \mu_{p_\pm} & C_{\kappa p_\pm}^\dagger & 0 \\ 0 & C_{\kappa p_\pm} & \mu_\kappa & 0 \\ 0 & 0 & 0 & H_\eta \end{pmatrix}, \quad (\text{B14})$$

where the four blocks correspond respectively to the (τ, p_z) , (τ, p_\pm) , (κ, s) , and (η, p_\pm) orbitals. The chosen parameters for the relative strengths of the terms are provided in Table VI. Note that, if we switch off all the perturbations other than H_η , the two bands at charge neutrality will remain exactly flat.

Appendix C: Deformation to explicit atomic limits for the six-band model

For completeness, we demonstrate the triviality of the complementary bands in the six-band model in this appendix. Unlike the ten-band model, our six-band model was defined using only conventional hopping terms without resorting to the notion

of quasi-orbitals. Consequently, the four complementary bands are not automatically trivial. This can be settled by a similar deformation to an explicit atomic limit, achieved by first augmenting the Hilbert space to include the (η, p_{\pm}) bands, and then writing down a deformation Hamiltonian akin to that in Eq. (4) in the main text:

$$H'_{\mu}^{(6)} = t_0 \cos\left(\frac{\pi\mu}{2\mu_0}\right) \begin{pmatrix} 0 & \tilde{h}_{\mathbf{k}} \\ \tilde{h}_{\mathbf{k}}^{\dagger} & 0 \end{pmatrix} + \mu \begin{pmatrix} \frac{1}{\mu_0} H^{(6)} & 0 \\ 0 & \frac{1}{10} \mathbb{1} \end{pmatrix}. \quad (\text{C1})$$

Here, $\tilde{h}_{\mathbf{k}}$ is identical to that defined in Appendix B 2, but with a different set of wave-function parameters $(a, b, c, d) = (0.48 - 0.24i, 0.13 + 0.42i, 0.04 + 0.30i, 0.24 - 0.29i)$. As before, we set $t_0 = \mu_0 = 130$ meV.

When $\mu = \mu_0$, the lowest four bands coincide with that of $H^{(6)}$; when $\mu = -\mu_0$, the lowest four bands correspond to the strict atomic insulator arising from the (η, p_{\pm}) orbitals. In Fig. 7, we plot the evolution of the band gap between the fourth and fifth bands. The gap never closes, which establishes a smooth deformation of the lowest four bands of $H^{(6)}$ to a strict atomic insulator.

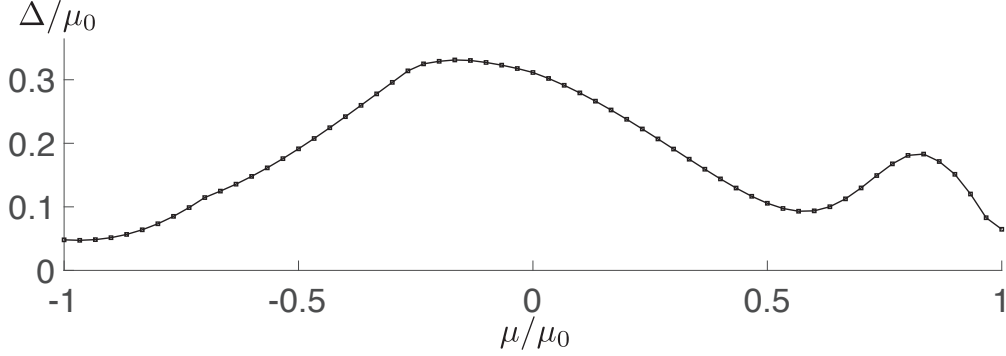


FIG. 7. Evolution of the band gap between the fourth and fifth bands of Eq. (C1), which establishes an adiabatic deformation of the lowest four bands of our six-band model to a strict atomic insulator. More than 2.4×10^4 momenta are sampled in the BZ.

Appendix D: “Wilson loop” analysis

In Ref. 55, it was proposed that the band topology of the two nearly flat bands of TBG could be inferred from a certain topological property of the Wilson loop, and the authors further suggested that this band topology is “stable,” in that it will survive even in the presence of additional trivial degrees of freedom.

In essence, “Wilson loops” are the multi-band generalization of the Berry phase [56]. To be self-contained, we define it as follows: Consider a set of n bands whose eigenvectors are collected into a matrix $\Psi_{\mathbf{k}}$ for every \mathbf{k} . Let \mathcal{C} be a closed path in the BZ, and let $\{\mathbf{k}_i\}$ be a discretization of \mathcal{C} into N momenta such that $|\mathbf{k}_{i+1} - \mathbf{k}_i| \rightarrow 0$ as $N \rightarrow \infty$. We further label the momenta such that $\mathbf{k}_N = \mathbf{k}_1 + \mathbf{b}$, where \mathbf{b} (possibly = $\mathbf{0}$) is a reciprocal lattice vector encoding the topological property of \mathcal{C} (as a loop over the BZ). Then we define the Wilson loop to be the $n \times n$ matrix

$$\mathcal{W}(\mathcal{C}) \equiv \lim_{N \rightarrow \infty} \Psi_{\mathbf{k}_1}^{\dagger} \Psi_{\mathbf{k}_2} \Psi_{\mathbf{k}_2}^{\dagger} \dots \Psi_{\mathbf{k}_{N-1}} \Psi_{\mathbf{k}_{N-1}}^{\dagger} \Psi_{\mathbf{k}_N}, \quad (\text{D1})$$

where care must be taken to relate $\Psi_{\mathbf{k}_N} = \mathcal{U}_{\mathbf{k}_1, \mathbf{b}} \Psi_{\mathbf{k}_1}$ for some unitary matrix $\mathcal{U}_{\mathbf{k}_1, \mathbf{b}}$. $\mathcal{W}(\mathcal{C})$ is unitary when $N \rightarrow \infty$, and in the presence of $\mathcal{C}_2\mathcal{T}$ symmetry it can be further shown to be orthogonal [53, 55, 56].

Following the recipe in Ref. 55, we compute $\mathcal{W}(\mathcal{C})$ for a particular set of contours: write any \mathbf{k} in the BZ as $\mathbf{k} = \frac{k_{\parallel}}{2\pi} \mathbf{b}_{\parallel} + \frac{k_{\perp}}{2\pi} \mathbf{b}_{\perp}$, where \mathbf{b}_{\parallel} and \mathbf{b}_{\perp} are distinct reciprocal lattice vectors. Then pick \mathcal{C} to be “straight lines” running along \mathbf{b}_{\parallel} wrapping around the BZ once. The different contours are then labeled by the remaining coordinate k_{\perp} , and one studies the properties of the family of Wilson loops $\{\mathcal{W}(k_{\perp}) : k_{\perp} \in [0, 2\pi)\}$.

We compute this Wilson loop spectrum for our ten-band model $H(t_0, \delta_0)$ (Eq. (3) in the main text), choosing $\mathbf{b}_{\parallel} = \mathbf{b}_2$ and $\mathbf{b}_{\perp} = \mathbf{b}_1$. The results are shown in Fig. 8. As shown in Fig. 8a, we find the same nontrivial spectral flow for the nearly flat bands as in Ref. 55. This is expected, as it is quite likely that the \mathbb{Z} -valued Wilson loop invariant suggested in Ref. 55 (arising from $\pi_1(O(2)) = \mathbb{Z}$, as was noted earlier in Ref. 53), is equivalent to the chirality obstruction we identified in Ref. 28.

Fig. 8b shows the spectrum obtained for the lowest four bands, which, as we have shown, are adiabatically connected to an explicit atomic insulator. Note the existence of continuous spectral gaps between the bands, which implies the Wilson loop invariant is trivial, as is consistent with the atomic nature of the bands

Fig. 8c shows the spectrum for the lowest six bands, i.e., the composite bands formed by those in (a) and (b). Importantly, a continuous spectral gap is also found, again consistent with the fact that these six bands together form an atomic insulator.

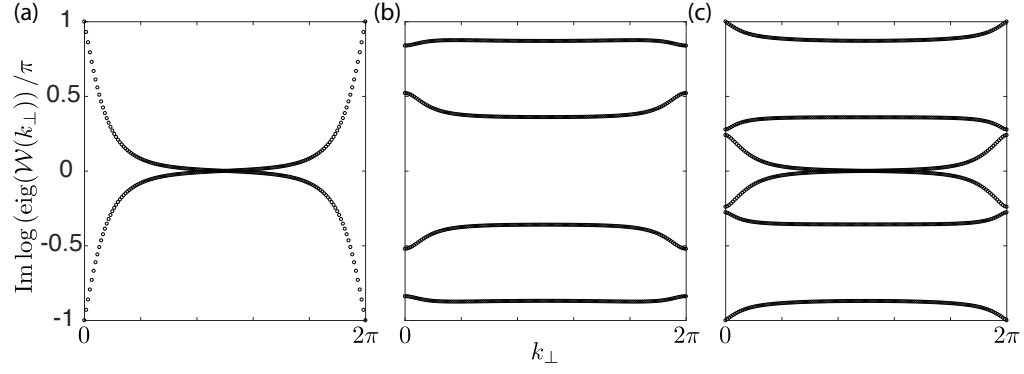


FIG. 8. Wilson loop spectra computed following the scheme described in Ref. 55, for the following set of bands: (a) the two nearly flat bands at charge neutrality; (b) the lowest four bands; and (c) the six bands of (a) and (b) combined. Note that a nontrivial spectral flow is found only in (a), consistent with the fragile nature of the band topology.